

Collapsing bacterial cylinders

M. D. Betterton^{1,*} and Michael P. Brenner²

¹*Department of Physics, Harvard University, Cambridge, Massachusetts 02138*

²*Division of Engineering and Applied Science, Harvard University, Cambridge, Massachusetts 02138*

(Received 20 August 1999; revised manuscript received 20 June 2001; published 13 November 2001)

Under special conditions bacteria excrete an attractant and aggregate. The high density regions initially collapse into cylindrical structures, which subsequently destabilize and break up into spherical aggregates. This paper presents a theoretical description of the process, from the structure of the collapsing cylinder to the spacing of the final aggregates. We show that cylindrical collapse involves a delicate balance in which bacterial attraction and diffusion nearly cancel, leading to corrections to the collapse laws expected from dimensional analysis. The instability of a collapsing cylinder is composed of two distinct stages: Initially, slow modulations to the cylinder develop, which correspond to a variation of the collapse time along the cylinder axis. Ultimately, one point on the cylinder pinches off. At this final stage of the instability, a front propagates from the pinch into the remainder of the cylinder. The spacing of the resulting spherical aggregates is determined by the front propagation.

DOI: 10.1103/PhysRevE.64.061904

PACS number(s): 87.18.Ed, 87.18.Bb, 87.18.Hf

The formation of a singularity—the divergence of a physical quantity in finite time—is central to diverse fields [1], including nonlinear optics, gravitational collapse, and fluid mechanics. The structure of singularities has been worked out in many examples for which a physical quantity blows up at a spatial point [2–4]. Typically, singular dynamics are self-similar: the characteristic scale separation between the singular and regular parts of the solution leads to the slaving of the spatial structure to the time dependence via scaling laws. The situation can be more complicated when many singularities form collectively and simultaneously. In this paper, we analyze a simple example for which multiple singularities form in a short time. This work was motivated by a recent experiment in bacterial chemotaxis [5–7].

The experimental observation is shown in Fig. 1. In the first panel a diffuse cloud of *Escherichia coli* (*E. Coli*) covers the depth of a Petri dish filled with agar. Note that even though this experiment takes place in a Petri dish with a thin agar layer, it is *not* quasi-two-dimensional, as shown in Ref. [7]. The dynamics in the thin direction are crucial to the pattern formation. Other experiments on bacteria have examined the case where the bacteria do not penetrate the agar [8]; our arguments do not apply to such experiments that are confined to two dimensions.

The environment is prepared so that the *E. coli* excrete an attractant; each bacterium attracts all the other bacteria, and a cloud can collapse. In the second panel, the diffuse cloud collapses as a cylindrical structure, with highest bacterial density on the cylinder axis. In the final panel, the cylinder breaks down into spherical aggregates. In this paper, we analyze the cylindrical collapse of bacteria and the stability of the collapsing cylinder.

Chemotaxis in *E. coli* provides a good model system for studying singularity formation. The biochemical response of *E. coli* to a changing environment has been well character-

ized [9–13] over the past 25 years, so we have a good understanding of how the bacteria sense and respond to their environment. As a consequence, it is possible to write down a “first-principles” hydrodynamic theory for the motion of many bacteria [14,15] in which the response coefficients are measurable. Quantitative comparison between theory and experiment is possible, and any discrepancies can be traced directly to the biochemistry of individual bacteria [7]. The application to singularity formation arose from the recent discovery by Budrene and Berg [5,6] of an assay in which *E. coli* excrete aspartate, an amino acid that is also an attractant

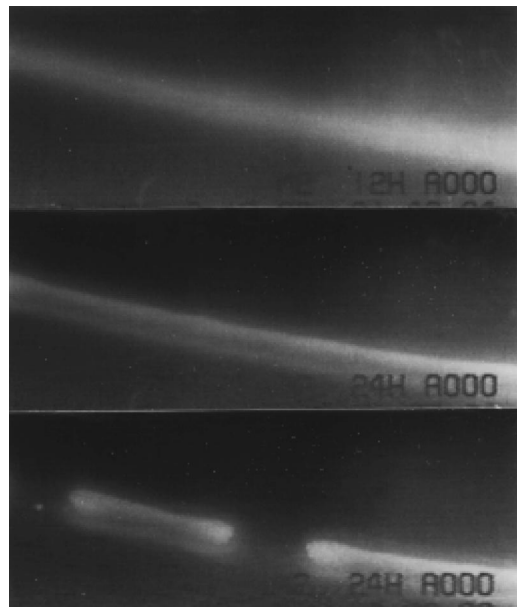


FIG. 1. Experiment showing formation and instability of a collapsing bacterial cylinder (reproduced from [7] with permission from the Biophysical Society). The first panel shows a diffuse cloud of bacteria filling the depth of a Petri dish filled with agar, which then collapses (second panel) into a cylindrical structure. The cylinder subsequently destabilizes into spherical aggregates. Details of the experiments are described in Budrene and Berg [5,6].

*Present address: Courant Institute, New York University, 251 Mercer St., New York, NY 10012.

for nearby bacteria. Attractant diffusion drives aggregation because it leads to an effective force between individual bacteria; a higher density of bacteria in a given region leads to higher attractant concentration, which drives a further increase in the bacterial density.

The initial interest in the Budrene-Berg experiment was stimulated by the symmetrical patterns (shown in Refs. [5,6]) that form when chemotactic bacteria are seeded in the center of a Petri dish. For a review of the large literature on bacterial colony development, see Ref. [8]. For the Budrene-Berg experiments in particular, several theories have been developed for these patterns, most of which [16–21] view the pattern formation as resulting from a linear instability of a (one-dimensional) traveling wave of bacteria. Recently, it was pointed out [7] that each of the aggregates in a pattern corresponds to a density singularity in the hydrodynamic description of the bacteria. Therefore, the pattern formation depends crucially on the dynamics of singularity formation. Singularities in chemotaxis were anticipated by Nanudjiah [22] and Childress and Percus [23] in studies of mathematical models of chemotaxis. An important feature, understood first by Childress and Percus, is that chemotactic collapse has a *critical dimension*: although collapse to an infinite density sheet is mathematically impossible, collapse to infinite density lines and points both can occur. It was argued in Ref. [7] that these facts crucially affect the patterns that can form.

In particular, Fig. 1 shows a step in the formation of aggregates. The initially diffuse band (filling the depth of agar) cannot form a singularity by collapsing only one of its dimensions to zero thickness; instead it collapses into a cylinder (contracting two of its dimensions simultaneously). The cylinder later destabilizes to form aggregates, for which all three dimensions contract simultaneously. Models [16–21] viewing aggregate formation as the linear instability of a band cannot account for these experimental observations. These two different pictures of how aggregates form lead to different conclusions about which biochemical parameters set the wavelength and structure of the patterns. For the “collapsing cylinder” mechanism advocated here, the characteristics of the pattern are set by the same biochemical cutoff that prevents an aggregate from reaching infinite density.

Cylindrical collapse is also important when an initially uniform-density cloud of bacteria breaks into aggregates. Linear stability analysis of the uniform-density state predicts that the cloud directly breaks down into spherical aggregates. However, experiments [24] find that the clumping is hierarchical: the uniform density cloud first collapses as cylindrical structures, which then break into spherical aggregates. An important unsolved issue is to explain the geometry of the high density regions during collapse, and to predict the final distribution of aggregates.

In this paper, we use a combination of simulations and asymptotics to describe the breakup of a cylinder in three principal steps (Fig. 2). First, the bacteria collapse as a cylinder towards a line of infinite density. In the second step, uniformity along the cylinder axis is broken, and a singularity develops at one point. Finally, the remaining cylinder breaks up, producing a sequence of spherical aggregates. Our

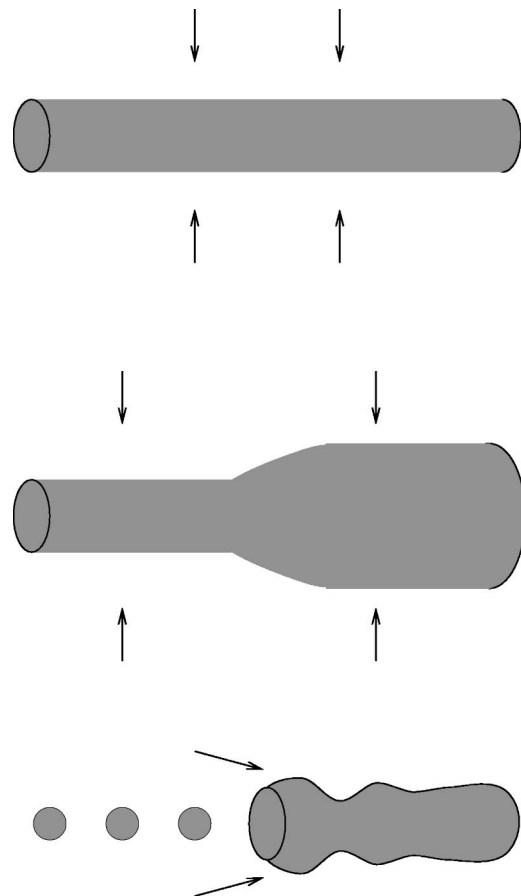


FIG. 2. Schematic (not to scale) of the three phases of cylindrical collapse. Top, a collapsing cylinder is formed. Middle, the cylinder becomes modulated. Bottom, the modulated cylinder pinches off and contracts, leaving a series of spherical aggregates. Note that this sketch does not show the radial contraction of the cylinder, which takes place as it collapses.

primary conclusion connecting the present theory with the experiments is that the final spacing between aggregates is determined by the local depletion of chemicals that make aspartate production possible. According to Budrene [24], oxygen is the most likely depleted quantity. This dependence of the aggregate spacing on initial overhead oxygen concentration in the cell could be directly tested in future experiments, and would serve to discriminate this theory from those based on pure linear stability analysis.

In the following section, we review the basics of chemotaxis, and discuss details necessary to understand the Budrene-Berg experiments. In Sec. II, we review previous results on chemotactic collapse. Section III describes our attempt to characterize the cylindrical collapse of the bacteria. Cylindrical collapse (in which two dimensions of the cloud contract simultaneously) is a critical case [23,25], for which diffusion and attraction nearly exactly balance. This criticality complicates attempts to solve the collapse. We attempted to verify numerically the solution for the cylindrical collapse proposed by Herrero and Velazquez [26]. We encountered numerical convergence difficulties that are described in Appendix B. In Sec. IV, we perform a stability analysis of a collapsing cylinder. Perturbations to the cylinder can be de-

scribed by a “phase equation” for the singular time [27]. Solutions to this envelope equation explain full numerical simulations of a modulated cylinder. Section V describes the final stage of the breakup of the cylinder, after the cylinder has pinched off at a point. Stability analysis predicts the breakup of the remaining column of bacteria, a situation analogous to a propagating Rayleigh instability in a liquid column [28]. We conclude with a comparison to experimental results and experimentally testable predictions.

I. BACTERIAL CHEMOTAXIS

Chemotaxis refers to the migration of bacteria up chemical gradients. For *Escherichia coli*, the basis of chemotaxis is largely understood [29,30]: in the absence of a chemical gradient, an *E. coli* bacterium performs a random walk [31]. When chemical gradients are present, the bacterium’s internal biochemical reactions detect the gradients and couple to the bacterial movement system. This sensing biases the random walk, and the bacterium has a net drift towards a chemical attractant. Under special conditions, the bacterium can excrete the chemoattractant aspartate [5,6] by converting carbon and nitrogen sources (succinate and ammonia, respectively) in its environment. In these experiments, no *external* chemical gradients are present. Instead, each bacterium moves in response to the attractant produced by other bacteria. Thus, the excretion of attractant produces a long-range force between the bacteria, and induces complicated interactions in the colony.

The equations for the collective motion of the bacteria can be derived (with no free parameters) from the underlying biochemistry [15], allowing quantitative comparison between theory and experiment. The basic equations for the bacterial density ρ and the attractant concentration c are

$$\frac{\partial \rho}{\partial t} = D_b \nabla^2 \rho - \nabla \cdot (k \rho \nabla c) + a \rho, \quad (1)$$

$$\frac{\partial c}{\partial t} = D_c \nabla^2 c + \alpha \rho. \quad (2)$$

Here D_b is the bacterial diffusion constant, k the chemotactic coefficient, a the rate of bacterial division, α the rate of attractant production, and D_c the chemical diffusion constant. The terms in Eq. (1) include the diffusion of bacteria, chemotactic drift, and division of bacteria. Equation (2) expresses the diffusion and production of attractant.

Equations of this type were first used to describe bacteria by Keller and Segal [32], and, with variations, have been the subject of extensive investigations (see, e.g., [33,34]). For *E. coli*, Schnitzer *et al.* [14] and Schnitzer [15] established the connection between the time-averaged properties of the bacterial response and the parameters in Eqs. (1), (2). Thus, the extensive studies of individual bacteria provide a justification for the equations, as well as measurements of the coefficients. There is one complication worth mentioning: Spudich and Koshland [35] showed that *E. coli* have “non-genetic individuality,” manifest in a distribution of tumble times (by about a factor of 2) between genetically identical bacteria. As

a consequence, both time-averaged and ensemble-averaged properties of the bacteria are necessary to predict hydrodynamic coefficients; in addition, the dynamics must be such that the distribution of bacteria in the ensemble does not change with time.

It is convenient to nondimensionalize Eqs. (1), (2) by choosing a characteristic density equal to the maximum initial density ρ_o . The characteristic scale of attractant is D_b/k . The density then determines the length scale and time scale according to $H = \sqrt{D_b D_c / (\alpha k \rho_o)}$ and $t_o = D_c / (\alpha k \rho_o)$. Typical numerical values are $D_b = 7 \times 10^{-6} \text{ cm}^2 \text{ sec}^{-1}$, $D_c = 10^{-5} \text{ cm}^2 \text{ sec}^{-1}$, $k = 10^{-16} \text{ cm}^5 \text{ sec}^{-1}$, and $\alpha = 10^3 \text{ sec}^{-1} \text{ bacteria}^{-1}$. For an experiment [7] that has $\rho_o = 10^6 \text{ cm}^{-3}$, the length scale is $260 \mu\text{m}$ and the time scale 100 sec. The equations become

$$\frac{\partial \rho}{\partial t} = \nabla^2 \rho - \nabla \cdot (\rho \nabla c) + \delta \rho, \quad (3)$$

$$\epsilon \frac{\partial c}{\partial t} = \nabla^2 c + \rho, \quad (4)$$

where $\epsilon = D_b/D_c$ and $\delta = a t_o$. For the experiments shown in Fig. 1, cells divide much more slowly than the collapse occurs; the time scale for cell division is $\approx 2 \text{ h}$, giving $\delta \approx 0.01$. Therefore, we set $\delta = 0$. The value of the parameter ϵ varies. For experiments in semisolid agar, the diffusion of bacteria is much slower than attractant diffusion, which motivates the limit $\epsilon = 0$ [7]. For experiments on bacteria in a liquid culture, $\epsilon \approx 1$. We will consider both limits in this paper. The $\epsilon = 0$ limit is convenient for asymptotic calculations. Our numerical simulations give results independent of ϵ in the range between 0 and 1.

For analytic calculations, working with the mass can be useful. For reference, we show the form of the equations here. Consider a radially symmetric density distribution, centered at the origin, which is symmetric in d directions. Define the mass contained within a radius r as

$$m(r) = \int dr r^{d-1} \rho. \quad (5)$$

This definition (and the choice $\epsilon = 0$) allows us to eliminate the concentration and write Eqs. (3), (4) as

$$\frac{\partial m}{\partial t} = r^{d-1} \frac{\partial \rho}{\partial r} + \rho m. \quad (6)$$

II. COLLAPSING SOLUTIONS

The equations for bacterial density and attractant concentration have collapsing solutions, for which the density goes to infinity in finite time. In the experiments, the density of bacteria does not become infinite. However, the density can increase by five orders of magnitude, and we expect that in the experiments the bacteria follow the collapsing solution up to some density cutoff. In this section, we introduce the types of allowed collapsing solutions. First we give heuristic arguments to explain why one-dimensional collapse (onto

planes) is not allowed, three-dimensional collapse (onto spheres) is possible, and two-dimensional collapse (onto cylinders) is marginal. We then review quantitative results. Because the length scale of density variations near a singularity is small, we can do asymptotics near the point where the density blows up. This leads to a similarity solution for the spherical collapse [36].

A. Critical dimension for collapse

The competition between diffusion and collapse leads to a critical dimension. In this problem, the critical dimension is 2, and one-dimensional collapse—collapse to a planar structure—is forbidden.

We make qualitative arguments to explain the critical dimension by comparing the chemotactic and diffusive fluxes in a contracting structure. For a sheet of thickness l , the inward diffusive flux is of order [see Eqs. (1), (2)]

$$J_D \sim -D_b \frac{\rho}{l}. \quad (7)$$

The chemotactic flux follows by integrating $D_c c'' \sim \alpha \rho$ (the prime denotes differentiation with respect to r) and defining M^{1D} as the mass per unit area of the planar region. Then the chemotactic flux is

$$J_C \sim k \rho c' \sim \alpha k \rho M^{1D} D_c^{-1}. \quad (8)$$

If the system collapses onto a plane, the thickness of the sheet $l \rightarrow 0$. The diffusive flux blows up while the chemotactic flux is unchanged. Thus a plane with small thickness is unable to reach infinite density, because diffusion eventually stops the collapse.

The situation is different for higher-dimensional structures. For symmetric spherical collapse (three directions contract simultaneously), the chemotactic flux is singular. When we balance $D_c \nabla^2 c \sim \alpha \rho$, we find $(r^2 c')' \sim \alpha r^2 \rho / D_c$. This implies a concentration gradient $c' \sim \alpha M^{3D} / (l^2 D_c)$, where M^{3D} is the mass contained within a sphere of radius l . The net inward flux of bacteria is then

$$J \sim \frac{-D_b \rho}{l} + \frac{\alpha k \rho M^{3D} D_c^{-1}}{l^2}. \quad (9)$$

As $l \rightarrow 0$, the inward flux (second term) dominates and collapse occurs.

In two dimensions, we encounter a subtlety. Assuming cylindrical collapse and repeating the dimensional argument, we have $(rc')' \sim \alpha r \rho / D_c$, and $c' \sim \alpha M^{2D} / (l D_c)$. (Here M^{2D} is the mass per unit length of the cylinder.) The inward flux is

$$J = \frac{-D_b \rho + \alpha k \rho M^{2D} D_c^{-1}}{l}. \quad (10)$$

Two-dimensional collapse is critical; the chemotactic and diffusive fluxes scale the same way with l . According to this simplified argument, there is a net inward flux if M^{2D}

$> D_c D_b / (\alpha k)$, which suggests that a system with mass above this critical value collapses.

B. Similarity solutions

We now quantify the preceding dimensional arguments and collect the known solutions to the chemotactic equations. As discussed above, the analytic solutions are derived with $\epsilon = 0$. First, consider one-dimensional collapse. Making the substitution [7,37] $v = \nabla c = \partial_x c$ in Eqs. (3), (4) implies

$$\frac{\partial v}{\partial t} = \frac{\partial^2 v}{\partial x^2} - v \frac{\partial v}{\partial x}. \quad (11)$$

This is the Burgers' equation; singular solutions to this equation do not exist [38].

In $d=2$ and higher, density singularities can develop. (Throughout this discussion, d refers to the number of simultaneously contracting dimensions.) In three dimensions, the nature of the blowup is straightforward. The characteristic length scale (L) varies in time, and the spatial structure is determined by the changes in L . A singularity corresponds to $L \rightarrow 0$. We guess the form of the similarity solution by balancing the different terms in Eqs. (3), (4). The diffusive dynamics imply $L = \sqrt{t^* - t} = \sqrt{\tau}$, with t^* the singular time and τ the time to singularity. Defining a dimensionless similarity variable $\eta = r/L$, we find the scaling form of the density, concentration, and mass by balancing all terms in the equations

$$\rho = \frac{1}{L^2} R(\eta), \quad (12)$$

$$c = C(\eta), \quad (13)$$

$$m = L^{d-2} M(\eta). \quad (14)$$

In writing this form of solution, we have assumed radial collapse at the origin ($r=0$). For a similarity solution to be valid, it must obey the correct boundary conditions: the density ρ and the attractant concentration c must be time-independent far from the singularity, which requires $R \sim \eta^{-2}$ and $C \sim \text{constant}$ as $\eta \rightarrow \infty$.

Plugging in the scaling form gives an ordinary differential equation in the similarity variable η , where here the prime denote differentiation with respect to η :

$$\frac{\eta M'}{2} = \eta^{d-1} R' + R M, \quad (15)$$

$$\eta^{d-1} R = M'. \quad (16)$$

In $d=3$, the similarity equation can be solved exactly; the one stable solution, found by Kadanoff [36], is

$$R = \frac{4(3 + \eta^2)}{(1 + \eta^2)^2}. \quad (17)$$

As demonstrated in Ref. [36], this similarity solution agrees well with numerical solutions.

III. CYLINDRICAL COLLAPSE

In this section we describe the two-dimensional collapsing solution of the evolution equations. As shown below, a solution to the similarity equations (15), (16) that satisfies the necessary boundary conditions is not possible when $d = 2$. Nevertheless, a collapsing solution with a density singularity does exist [25]. Here we describe our attempt to simulate the cylindrical collapse. Our work on this problem was complicated by numerical difficulties, leading us to conclude that our numerical scheme has not converged. (We discuss the numerics in more detail in Appendix B.) Because of these problems, we are unable to evaluate the form of the logarithmic correction to the collapse scaling laws. Here we give an outline of the basic features of the cylindrical collapsing solution, and leave the full numerical solution as an open problem.

Herrero and Velazquez [26] used formal asymptotics to construct the solution for a collapsing cylinder, and proposed the form of the logarithmic correction. We see the qualitative features of the Herrero-Velazquez solution in our numerics; however, we are unable to verify their form of the logarithmic correction.

In two dimensions, there is no solution to Eqs. (15), (16) that satisfies the boundary conditions. To see this, note that for $d=2$ the similarity equations can be integrated to give

$$R = e^{\eta^{3/4}} \exp\left(\int \frac{M}{\eta}\right). \quad (18)$$

This form for R cannot satisfy the boundary conditions that the density and mass be stationary at large η , because R grows without bound as $\eta \rightarrow \infty$.

Nevertheless, a similarity-type solution to the equations exists, the basic features of which we can capture in a simulation, as shown in Fig. 3. (The numerical method is described in Appendix A; its most important feature is the mesh refinement, which frequently moves mesh points to better resolve the singularity [39].) As the simulation progresses, the maximum density increases. When we examine the scaling of the maximum density and the length scale L , we find $\rho \sim L^{-2}$ and $L \sim \sqrt{\tau}$, as expected for a similarity solution.

How can this be consistent with the argument that no similarity solution exists? We believe that corrections to the similarity solution arise to solve this problem. Although the basic self-similar scaling $\rho_m \sim L^{-2}$ is preserved, the time dependence of L can be different than what the simple dimensional argument suggests. This leads to slow (logarithmic) time dependence of $L/\sqrt{\tau}$.

The structure of the solution is shown in Fig. 4, where the curves have been collapsed by rescaling the density and the radius. As $L \rightarrow 0$, the inner collapsing region converges to a *pseudostationary* solution, which has the same spatial dependence as the stationary ($\partial\rho/\partial t = \partial c/\partial t = 0$) solution to the original equations (3), (4). The pseudostationary solution scales as $\rho \sim \eta^{-4}$ for large η , as shown in the figure. The

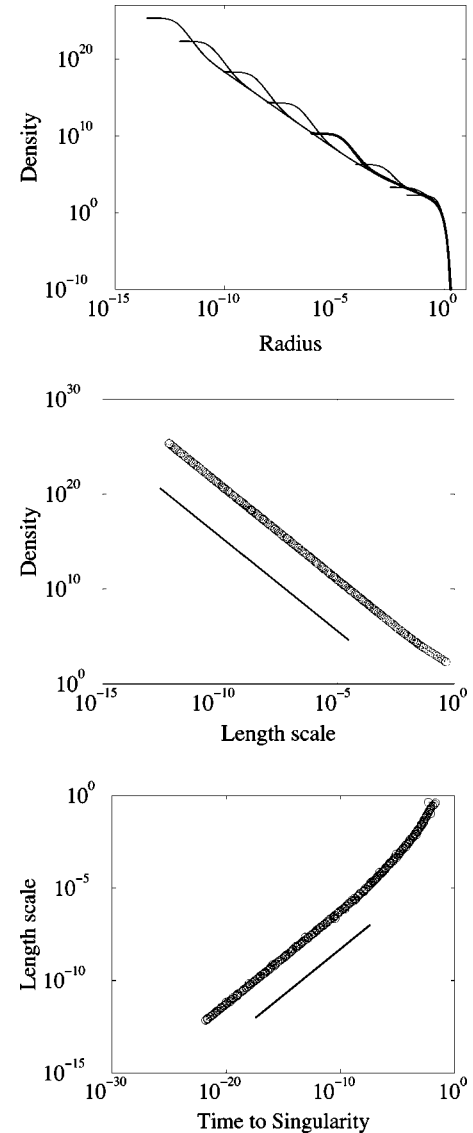


FIG. 3. Cylindrically collapsing solution. Top, density as a function of radius for the cylindrical simulation. The different curves correspond to different times. Middle, the maximum density vs characteristic length scale. The solid line has exponent -2 . Bottom, the length scale of the cylinder vs time to the singularity τ . The solid line has exponent 0.5 . The length scale is defined as the radius where the density decreases from its maximum by a factor of 5.

inner region matches onto an outer region where $\rho \sim \eta^{-2}$, as required for the collapsing solution to be stationary far from the origin. The inner pseudostationary solution has a dimensionless mass of 4. Thus, the evolution of the collapse has a specific physical interpretation. In dimensionless (similarity) variables, the inner region expels excess mass to approach $M=4$. Matching between the inner and outer regions should determine the dynamics.

To illustrate the nature of the nearly self-similar solution, we define the collapse rate $A(t) = -\dot{L}L$. (Note that the collapse rate of the system is \dot{L}/L ; we can make a dimensionless collapse rate by multiplying by the time scale $\tau \sim L^2$.) For exactly self-similar collapse, the collapse rate $-\dot{L}L = 1/2$ is a

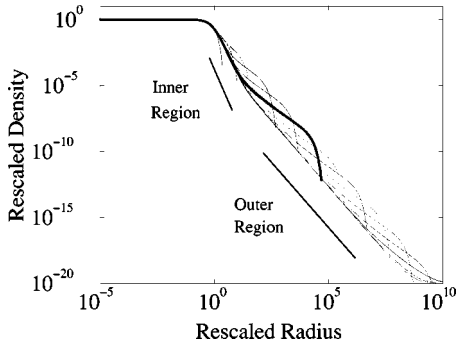


FIG. 4. Similarity profiles. The density divided by the maximum density vs the similarity variable $\eta = r/L$. The different curves are the same as those shown in the previous figure. The solid line in the inner region is a power law with exponent -2 ; the line in the outer region has exponent -4 .

constant. In the presence of corrections, the collapse rate goes asymptotically to zero.

We rewrite the similarity equations assuming that M and R depend on the similarity variable η and (slowly) on time. The similarity equations are then

$$L^2 \frac{\partial M}{\partial t} + A \eta M' = \eta R' + RM, \quad (19)$$

$$\eta R = M'. \quad (20)$$

Note that here the time derivative of M refers only to *explicit* time dependence of the mass; the second term takes into account the time dependence slaved to the varying length scale.

We can solve the similarity equations in the inner region. As the collapse proceeds, it slows down. This motivates us to look for a solution with $A=0$; that is, a pseudostationary solution (in similarity variables). This pseudostationary solution solves Eqs. (19), (20) when $A=0$ and $\partial_t M=0$. The equation for the mass is then

$$\eta M'' + M'(M-1) = 0. \quad (21)$$

Exact solutions to this equation are

$$R_0 = \frac{8}{(1 + \eta^2)^2}, \quad (22)$$

$$M_0 = \frac{4\eta^2}{1 + \eta^2}. \quad (23)$$

From the formula for M_0 we see an important feature of the stationary solution: the total mass is 4 in dimensionless units. This reflects a rigorous result [25,36]: collapse will occur if and only if the total mass per unit length of the cylinder satisfies $M > 4$. (For $M < 4$, no collapse is possible—the system evolves to a constant density.) When $M > 4$, collapse occurs; the solution converges toward a collapsing mass precisely equal to 4. In similarity variables, therefore, mass flows away from the origin.

Compare this expression for R_0 to the numerical density profiles in Fig. 4. The shape of the profile confirms that the pseudostationary solution holds in the inner region. At large η , the stationary solution has $R_0 \sim \eta^{-4}$, while the boundary conditions require $R \sim \eta^{-2}$. The inner solution to the equations must, therefore, match an outer solution, as shown in Fig. 4.

Note that the crossover between inner and outer solutions will occur at some coordinate η_* , when $A \eta M' \sim A \eta^2 R \sim RM$ [see Eq. (19)]. This gives

$$\eta_* \sim A^{-1/2}. \quad (24)$$

The matching between inner and outer solutions leads to a length scale L of the form $L = \sqrt{\tau}/f(\ln \tau)$, where f is the correction to the dimensional scaling. An analysis of this matching was performed by Herrero and Velazquez [26]; their result gave the correction term

$$f(\ln \tau) = \frac{\sqrt{\tau}}{L} \sim \exp(\sqrt{2}/2 \sqrt{|\ln \tau|}). \quad (25)$$

We were unable to compare our numerical results to this formula; see Appendix B for details. In the remainder of this paper, we use the fact that the logarithmic correction exists, but the results do not require the exact form of $f(\ln \tau)$.

IV. EVOLUTION OF A MODULATED CYLINDER

A collapsing cylinder eventually breaks into spherical aggregates. In this section, we derive an envelope equation that describes how modulations to the cylinder evolve. The challenge is to describe a *collapsing* cylinder. Collapse amplifies initially small perturbations. Therefore, small variations along the cylinder (in density and the radial length scale) become large. We can perform a valid perturbation analysis by studying variations in the singular time t^* .

In the original similarity solution, the singular time t^* is undetermined; if t^* changes by a constant, the solution remains valid. Allowing slow spatial variation in t^* breaks this symmetry. Therefore, we expect the variation of t^* to produce slow dynamics in space and time. Because this mode is the most slowly decaying, it dominates the evolution of a cylinder. We derive a phase equation, an approach used in many problems when stability is governed by a slow mode associated with a broken symmetry [27]. Phase equations [40] were invented to understand problems such as convection, where the relevant symmetry is translation, and the stability analysis is relative to a traveling wave solution. Earlier research moved towards applying phase equations to singularities: in work on blowup in the semilinear heat equation, Keller and Lowengrub [41] derived a transformation from a blowing-up variable to one that vanishes, and they perturbed in the vanishing variable. Also in the context of the semilinear heat equation, Bernoff [42] has examined how the singular time varies along a cylinder.

We compare solutions of our phase equation to full numerics and show that the evolution of a modulated, collaps-

ing cylinder is well described by the simplified phase equation.

A. Derivation of a phase equation

Here we give a flavor of the derivation of the phase equation; for details see Appendix C. We seek an equation for the dynamics of $\tau(z,t) = t^* - t = t_0 + T(z,t) - t$. Slow variation requires that both $T'' \ll T'$ and $\dot{T} \ll 1$. Once the collapse time varies along the axis of the cylinder, the similarity functions R and C are no longer exact solutions to the equations. We write

$$R = R_0(\eta) + \delta R_1(\eta, z, t), \quad (26)$$

$$C = C_0(\eta) + \delta C_1(\eta, z, t), \quad (27)$$

where $\eta = r/L_r$, the radial length scale $L_r = \sqrt{\tau(z,t)}/f(\tau)$, and f is the (unknown) logarithmic correction. The perturbation parameter δ is of order L_r/L_z , where L_z is the scale of the density variation along the axis of the cylinder.

We apply this guess to Eqs. (3), (4), and expand in δ . The lowest-order equation gives the similarity equations (19), (20). At first order, we find an equation of the form

$$\begin{aligned} \Lambda(R_1, C_1) = & F(R_0, C_0)(\tau_t + 1) + G(R_0, C_0)\tau_{zz} \\ & + H(R_0, C_0)\frac{\tau_z^2}{\tau}, \end{aligned} \quad (28)$$

where τ_z is the derivative of τ with respect to z , and so on. On the left-hand side, a linear operator Λ is acting on R_1 and C_1 ; Λ comes from the linearization of the original equations. The right-hand side contains derivatives of the singular time multiplied by known functions of R_0 and C_0 .

Although R_1 and C_1 are unknown, the right-hand side is constrained by a solvability condition: any function that is annihilated by the adjoint of Λ must be orthogonal to the right-hand side. That is, if $\Lambda^\dagger g = 0$ for a nonzero g , then the inner product [43]

$$\langle g, \Lambda(R_1, C_1) \rangle = \langle \Lambda^\dagger g, (R_1, C_1) \rangle = 0. \quad (29)$$

Hence the right-hand side of Eq. (28) is orthogonal to g . In this problem (see Appendix C) precisely one nonzero g satisfies $\Lambda^\dagger g = 0$. Taking the inner products leads to a phase equation of the form

$$c_1(\tau_t + 1) + c_2\tau_{zz} + c_3\frac{\tau_z^2}{\tau} = 0, \quad (30)$$

where the constants c_1 , c_2 , and c_3 can be expressed in terms of the known functions g , F , G , and H :

$$c_1 = \langle g, F(R_0, C_0) \rangle, \quad (31)$$

$$c_2 = \langle g, G(R_0, C_0) \rangle, \quad (32)$$

$$c_3 = \langle g, H(R_0, C_0) \rangle. \quad (33)$$

As shown in Appendix C, for a modulated cylinder the phase equation is

$$\frac{\tau_t + 1}{f^2} = \tau_{zz} - \frac{\tau_z^2}{\tau}. \quad (34)$$

The logarithmic correction terms in this equation (the f^2 in the denominator) arise directly from the logarithmic corrections to the length scale in the two-dimensional solution. In the following section, we show that the logarithms lead to asymptotically different scalings for the radial and axial length scales of the collapsing cylinder. Hence, a ‘‘point’’ singularity that forms on a collapsing cylinder does not have the same collapse rate as a collapsing sphere. In the absence of logarithmic corrections to dimensional scaling, the phase equation is simply

$$\tau_t + 1 = \tau_{zz} - \frac{\tau_z^2}{\tau}. \quad (35)$$

B. Numerical simulations of a collapsing cylinder

Now we compare solutions of Eq. (34) with a fully nonlinear simulation of a collapsing cylinder. We have found two different mechanisms by which modulations of the cylinder can produce singularities: the first is a ‘‘point’’ singularity, in which the density blows up at a point on the cylinder; the second is a ‘‘traveling’’ singularity, which moves along the cylinder axis with a diverging velocity as the singularity is reached.

The primary technical difficulty in simulating a modulated collapsing cylinder is developing a remeshing algorithm to closely approach the singularity. The remeshing algorithm described here resolves density singularities along the axis of the cylinder with essentially arbitrary resolution. The algorithm is based on a simple one-dimensional scheme, which redistributes mesh points every 50 time steps to resolve the singularity. The two-dimensional algorithm uses the one-dimensional remeshing scheme along both \hat{r} and \hat{z} simultaneously; the two-dimensional equations are then solved by operator splitting. Details of the algorithm are summarized in Appendix A.

A typical simulation [44] started with a z -independent initial condition, which was allowed to progress until the maximum density reached 10^4 . At this point, the radial profile of the collapse was well approximated by the (two-dimensional) collapsing similarity solution seen in the two-dimensional simulation. We then added a z -dependent perturbation to the density profile, with amplitude much smaller than the ambient density.

The separation of scales hypothesis underlying the derivation of the phase equation is maintained uniformly in time. We experimented with different functional forms for the density perturbations; as long as the length scale L_z for variation in the z direction is longer than the variation in the radial direction L_r , perturbations tended to grow. In all cases, the relation $L_z \gg L_r$ was maintained. As demonstrated in Fig. 5, a radial cross section of the cylinder always revealed density

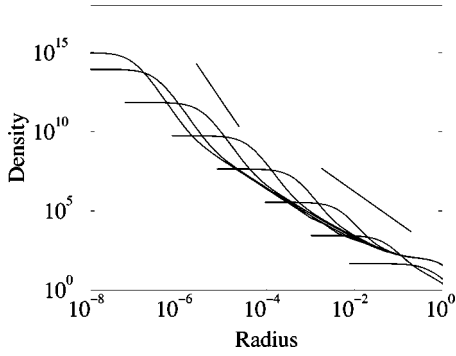


FIG. 5. Radial density profile at a single point on a modulated, collapsing cylinder. Note the r^{-4} region matched to the r^{-2} region: the solution is well described by the two-dimensional similarity solution throughout the collapse (cf. Fig. 3) even in the presence of a z -dependent modulation.

profiles in agreement with the two-dimensional collapsing solution.

1. Traveling singularity

Traveling singularities occur when a steplike perturbation is placed on the cylinder, increasing the density for $z < z_0$ and decreasing the density for $z > z_0$. The subsequent evolution occurs at the boundary between these two regions. A simulation of this process is shown in Fig. 6. We find that the boundary propagates toward the higher density. Heuristically, the higher-density region is beginning to contract as a sphere, so its decrease in size is consistent with the beginning of spherical collapse.

This propagating singularity can be described as a solution to the phase equation (34) of the form

$$\tau = \tau_0 \phi[z - z_0(t)], \quad (36)$$

where $\tau_0 = t^* - t$ is the basic phase expected from collapse. All the nontrivial space and time dependences are absorbed in ϕ and z_0 . Inserting into the phase equation, we have

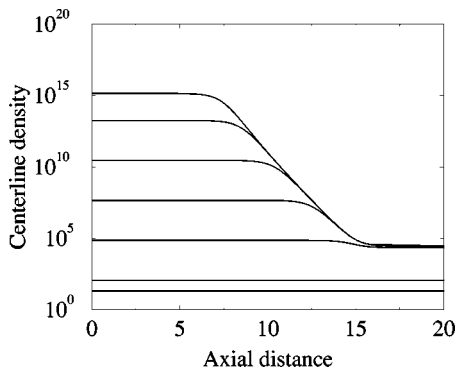


FIG. 6. Time evolution of the centerline density $\rho(r=0,z)$, with a steplike initial condition. The perturbation is seeded when $\rho = 10^4$. The highest-density region *propagates* to the left. Hence, the spatial extent of the high-density region shrinks as the collapse is approached. Note that $\tau(z) \sim \rho(r=0,z)^{-1}$.

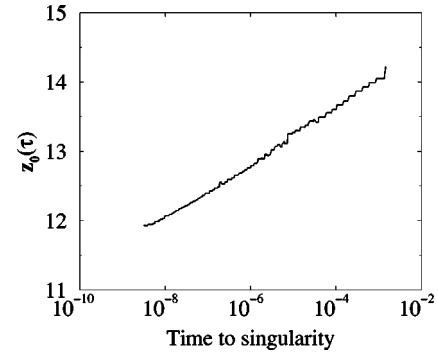


FIG. 7. Location of the edge of the maximum density region $z_0(\tau)$ as a function of time. As predicted by the theory, the edge moves according to the law $z_0(\tau) = -A_{vel} |\ln \tau|$. Regression gives $A_{vel} \approx 0.17$.

$$\frac{\dot{\tau}_0 \phi - \dot{z}_0 \tau_0 \phi' + 1}{f^2} = \tau_0 \left(\phi'' - \frac{\phi'^2}{\phi} \right). \quad (37)$$

The right-hand side of this equation is $O(\tau_0)$, which becomes arbitrarily small as the singularity is approached. Therefore, the left-hand side must be equal to zero, which gives

$$\dot{\tau}_0 \phi - \dot{z}_0 \tau_0 \phi' + 1 = 0. \quad (38)$$

In this equation, $\dot{z}_0 \tau_0$ must be independent of time. If we demand the balance $\dot{z}_0 \tau_0 = -A$, so the high-density region propagates to the left (decreasing z). Then

$$z_0 = A \ln \tau_0 = -A |\ln \tau_0|.$$

The solution for ϕ is then

$$\phi(\eta) = 1 + e^{+z/A}. \quad (39)$$

Figure 6 shows the density along the centerline of the cylinder. The decay of the highest density is exponential, as predicted by the phase-equation solution constructed above. A fit to the numerical data shows that

$$\rho(r=0,z) \sim e^{(-z/A_{pr})} \sim e^{(-3.1z)}, \quad (40)$$

yielding $A_{pr} = 0.32$, the value of A measured from the profile shape.

Figure 7 shows the location of the edge of the maximum density region $z_0(\tau)$ as a function of τ . As predicted by the phase equation analysis, the figure shows that $z_0 = -A |\ln \tau|$. A least squares fit gives the prefactor A (as measured from the front velocity) $A_{vel} \approx 0.17$. The qualitative features of the numerical simulations are thus in good agreement with the theory. Quantitatively, however, there is a discrepancy: the theory predicts that we should have $A_{vel}/A_{pr} = 1$, while our numerical simulation gives $A_{vel}/A_{pr} \approx 0.5$. We believe that the discrepancy arises because the convergence of our numerical scheme requires that we keep a small $\epsilon \approx 0.1$, while the analysis in the previous subsection assumes $\epsilon = 0$.

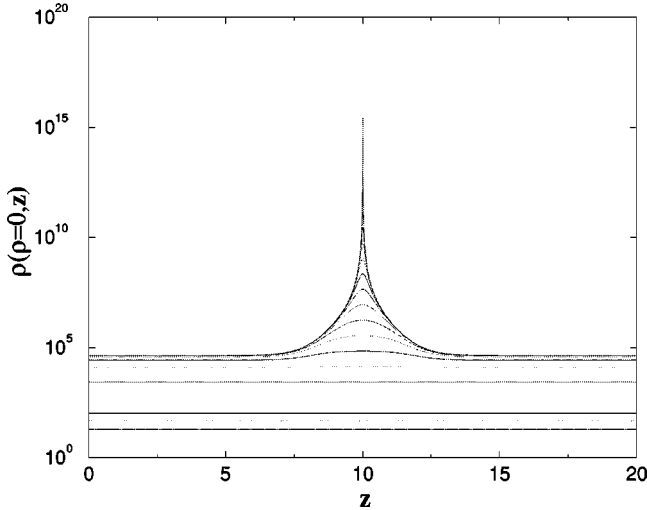


FIG. 8. Time evolution of the centerline density $\rho(r=0,z)$ for a point singularity. The singularity was initiated by placing a perturbation (symmetric about $z=10$) on a uniformly collapsing cylindrical solution.

2. Point singularity

Stationary singularities—blow-up at a spatial point—occur in the numerics for a wide variety of initial conditions. We believe that the stationary singularity represents the generic evolution of a modulated cylinder. Indeed, it is the end state of the traveling solution just discussed, when the propagating wave runs into the reflection-symmetric boundary condition. An instance of this solution is depicted in Fig. 8.

In contrast to the traveling singularity, the logarithmic corrections to the scaling laws are important in this solution. For our analysis, we take the point of blow-up to be at $z=0$. Satisfying the equation requires that the z length scale incorporate corrections to the scaling:

$$\tau = \tau_0 \phi \left(\frac{z}{\tau_0^\gamma h(\tau)} \right) = \tau_0 \phi \left(\frac{\xi}{h} \right), \quad (41)$$

where we have defined the similarity variable $\xi = z/\tau_0^\gamma$. The phase equation becomes

$$f^{-2} \left[-\phi + \frac{\xi}{h} \phi' \left(\gamma + \frac{\tau_0}{h} \frac{\partial h}{\partial \tau} \right) + 1 \right] = \tau_0^{1-2\gamma} h^{-2} \left(\phi'' - \frac{\phi'^2}{\phi} \right). \quad (42)$$

Demanding that the two sides scale the same way in time (and ignoring the $\tau_0 h'/h$ term because it is negligibly small close to the singularity), we have

$$\frac{1}{f^2} = \frac{\tau_0^{1-2\gamma}}{h^2}, \quad (43)$$

which gives $\gamma = 1/2$ and $f = h$. Thus $L_z \sim \tau_0^{1/2} f$, which differs from the radial length scale $L_r \sim \tau_0^{1/2} f^{-1}$. The result is

$$\frac{L_z}{L_r} = f^2. \quad (44)$$

This shows that the generic density singularity that forms during the breakup of cylindrical collapse is *not* spherical collapse, but something milder. Locally, since the axial scale L_z is much larger than the radial scale L_r , the structure still looks like a cylinder. Numerical evidence for this behavior is shown in Fig. 8 (although we note that the plots show behavior during an initial transient shown in Fig. 11 and discussed in Appendix B). The singularity develops a length scale in the axial direction that is much larger than the radial scale $1/\sqrt{\rho}$. For example, in Fig. 8, when $\rho = 10^{10}$ (so $L_r = 10^{-5}$), we find $L_z \sim 10^{-2}$. Our numerical algorithms unfortunately have not allowed us to find the asymptotic L_z/L_r numerically; the problem is that the separation of scales is so great between the radial and axial scales that one needs many more mesh points than we can afford to resolve the asymptotic regime.

V. BREAKUP INTO SPHERICAL AGGREGATES

The question of relevance to the experiments is what happens next. Once blowup occurs at a spatial point the cylinder has a free end, which changes the nature of the collapse. We can no longer use the strategy of the previous section—perturbation about a collapsing cylinder—because the radial structure is no longer closely approximated by the cylindrical solution. The pinchoff drives the dynamics; specifically, the pinched end of the cylinder forms a traveling wave. Heuristically, note that an “edge” of bacteria produces a higher concentration of attractant where the density is higher. Thus the “tail” of bacteria moves toward higher attractant density, and a traveling wave can form. Recall that for variation in one spatial dimension the equations reduce to the Burgers’ equation, which has traveling wave solutions [38]. The contraction of a cylinder end has been observed for the bacteria [24], and the traveling waves have been discussed in other contexts [7]. Here we discuss the instability of the recoiling end and the final spacing of the spheres.

Note the qualitative similarity between this instability and the Rayleigh instability of a liquid column [28]. The Rayleigh instability is driven by surface tension, and causes a cylinder of liquid to break up into spherical drops. This problem is similar, although more complicated. First, the cylinder is *collapsing*. The collapse is not present in the Rayleigh instability, and necessitates a different type of perturbation analysis. Second, this problem has no surface—the density varies smoothly. The instability is driven by interactions of the bacteria inside the cylinder.

Figure 9 shows a set of plots of a retracting cylinder. The simulation shows that the end of the cylinder collapses as a spherical aggregate, and simultaneously, in front of the aggregate waves travel into the bulk of the cylinder. The collapse of a single aggregate corresponds to formation of a singularity in the numerics. In order to continue beyond this singularity and simulate the formation of an array of aggregates, we introduced a cutoff that emulates the biochemistry

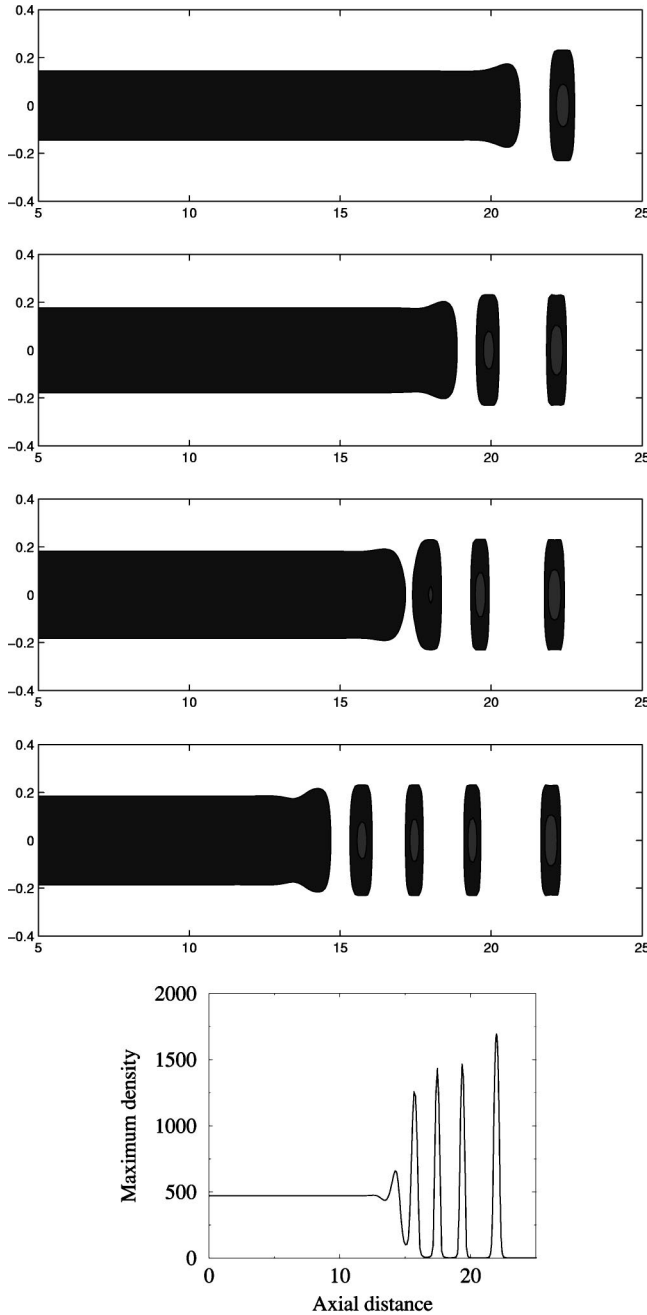


FIG. 9. Numerical simulation of a collapsing cylinder with a free end, showing contour plots of the density. As the cylinder recoils, aggregates are left behind. The spacing between the aggregates is determined by the density of the cylinder as it collapses. (Note that the value of the density corresponding to the black contour changes between frames, because the density in the cylinder increases with time.) The final frame in this figure shows the density profile along the centerline of the cylinder for the last contour plot (with four aggregates). The maximum density is near the cutoff density $\rho_* = 500$ discussed in the text.

in the experiment: when the bacterial density becomes too high, the bacteria locally deplete chemicals such as succinate and oxygen and cease to produce the attractant aspartate. We modeled this by changing the equation for c to

$$\frac{\partial c}{\partial t} = D_c \nabla^2 c + \alpha \rho e^{-\rho/\rho_*}. \quad (45)$$

If the density of bacteria is higher than the cutoff density ρ_* , the bacteria stop producing attractant. This prevents collapse to infinite density by limiting the increase in the gradient of attractant. In Ref. [7] this cutoff density was estimated (assuming the cutoff was caused by oxygen depletion) and shown to vary exponentially with the overhead oxygen concentration in the cell: $\rho_* \sim e^{C_{O_2}}$. For the simulation shown in Fig. 9, this cutoff $\rho_* = 500$. Note that the density of the (undisturbed) cylinder in front of the retracting rim slowly approaches the cutoff density ρ_* ; we have found in simulations that the undisturbed cylinder always collapses to a density close to the cutoff value.

The formation of the density wave occurs because the retracting end perturbs the cylinder in front of it. We can find the time-evolution of perturbations to the cylinder, requiring that they decay away from the free end. The most unstable mode can be found using the method of stationary phase [45]. If the linear growth rate is $\omega(q)$, the point of stationary phase q_* satisfies

$$\text{Im} \left. \frac{d\omega}{dq} \right|_{q_*} = 0, \quad (46)$$

$$\text{Re} \left. \frac{d\omega}{dq} \right|_{q_*} = \frac{\text{Re}(\omega)}{\text{Im}(q)}. \quad (47)$$

For the discussion here, we perform the calculation using the free-space dispersion relation. A perturbation to constant density that satisfies the boundary condition that the perturbation decay to zero at large positive z has the form

$$\rho = \rho_0 + \delta e^{\omega t - qz}, \quad (48)$$

$$c = \rho_0 t + \chi e^{\omega t - qz}, \quad (49)$$

where we have taken $\epsilon = 1$ for simplicity in this calculation. Plugging into the equations and linearizing gives the dispersion relation

$$\omega = \pm i \sqrt{\rho_0} q + q^2. \quad (50)$$

The most unstable mode is, in dimensionless units,

$$v_* = \mp \sqrt{\rho_0}, \quad (51)$$

$$q_* = \mp \frac{\sqrt{\rho_0}}{2} (1 + i), \quad (52)$$

$$\omega_* = \frac{\rho_0}{2}. \quad (53)$$

These formulas demonstrate that the wavelength of the modulations is determined by the undisturbed density in the bulk of the cylinder. Since this density increases to the cutoff density ρ_* , it follows that the wavelength of the ripples is determined by the cutoff. Thus the biochemical parameter

controlling the maximum density also determines the characteristic distance between aggregates. This conclusion can be experimentally tested.

The predictions for the wavelength and velocity of the front compare well with numerical simulations. On decreasing ρ_* from 500 to 140, the wavelength of the ripples increases from 1.4 to 2.5, in qualitative agreement with the formulas.

We remark that the basic scenario outlined in this section was discovered by Budrene, in unpublished experiments [24]. After observing the traveling band collapse as a cylinder (Fig. 1) Budrene observes fast “waves” propagating around the cylinder. Then, a fragmentation front moves along the collapsing cylinder, leaving spherical aggregates behind. The present theory predicts a scenario that is qualitatively similar: the fast “waves” correspond to the modulations of the cylinder described by the phase equation (i.e., the traveling steps, described in Sec. IV A). The fragmentation front occurs due to the propagating instability outlined in this section. Unfortunately, it is not currently possible to make a quantitative comparison of the experiments to the present theory, though such a comparison would prove interesting.

VI. CONNECTION TO EXPERIMENTS

This paper has shown how the patterns formed by *E. coli* are connected to the geometry of singularity formation in the hydrodynamic description of the bacteria. We have sketched the features of the solution for critical (two-dimensional) collapse, and developed a theory for modulations to the cylinder. The phase equation provides a useful simplified description of a perturbed cylinder. We argued that, ultimately, the spacing of spherical aggregates is determined by the instability of a pinched cylinder of bacteria.

Here we compare our work to published experiments and suggest tests of the theory. Not all the coefficients in the original equations (1) and (2) have been precisely measured [7] for the experimental regime of interest. In particular, neither the attractant production rate α nor the chemotactic coefficient k have been measured for bacteria in the same chemical environment as that of the collapse experiments. Thus, at this stage, we can make only order of magnitude numerical comparison with experiments. Here we use the values of the coefficients for bacteria in a liquid medium [7]: bacterial diffusion coefficient $D_b = 7 \times 10^{-6} \text{ cm}^2 \text{ sec}^{-1}$; attractant diffusion coefficient $D_c = 10^{-5} \text{ cm}^2 \text{ sec}^{-1}$ [46]; chemotactic coefficient $k = 10^{-16} \text{ cm}^5 \text{ sec}^{-1}$; and attractant production rate $\alpha = 10^3 \text{ sec}^{-1} \text{ bacteria}^{-1}$.

An important prediction of this theory is the critical mass of bacteria for cylindrical collapse. With the chosen parameter values, the formation of a collapsing cylinder requires a minimum number of bacteria per unit length $M = 4D_b D_c / (k\alpha) = 3 \times 10^3 / \text{cm}$. The existence of a critical number of bacteria for cylindrical collapse has been inferred from experiments [7], but this number has never been directly measured. We emphasize that (with experimental measurements for the parameters D_b , k , and α) the theory rigorously and precisely predicts this critical mass, allowing a direct test of the theory.

In this paper, we have discussed the logarithmic corrections in two-dimensional collapse. In the experiments, the subtle corrections to the dimensional scaling laws are probably not directly observable. However, the basic scaling relations expected from the similarity solution—for example, that the maximum density is related to the length scale of density variations by $\rho_m \sim L^{-2}$ —could be measured in experiments, both for cylindrical and spherical collapse. So far, no quantitative and controlled measurements of the bacterial density have been performed.

To our knowledge, modulations of a collapsing cylinder have never been quantitatively measured in experiments (although as mentioned above, Budrene has made qualitative observations of this effect). The traveling and point singularities that we predict for a modulated cylinder may be observable. In particular, we predict that the radial and axial length scales should be different for the point singularity. Because the difference in these length scales arises from the corrections in two-dimensional collapse, a measurement of these length scales would verify the existence of slow corrections.

The modulated cylinder ultimately pinches off at a point. We have argued that the spacing of spherical aggregates is determined by the instability of a cylinder with an end. In practice, when does the modulated cylinder pinch off (forming an end)? To answer this question, we must know when our theory breaks down. Collapse to infinite density cannot happen for bacteria, because they have finite size. It was argued in Ref. [7] that even before the hard packing density of bacteria is reached, oxygen depletion will stop the collapse. Regardless of the specific mechanism, at some time the highest-density part of the cylinder—the point singularity—will stop collapsing. This is the time of pinch-off, because the point singularity evolves much more slowly than do the neighboring, less dense regions of the cylinder.

This argument gives a testable prediction of our model, because the spacing of aggregates depends on the maximum density of the cylinder. In dimensional units, the most unstable wavelength (and, therefore, the aggregate spacing) is

$$\lambda = 4\pi \sqrt{\frac{D_b D_c}{\alpha k}} \rho_m^{-1/2} = 300 \text{ cm}^{-1/2} \rho_m^{-1/2}, \quad (54)$$

where we have used values of the coefficients from above. Thus, varying the maximum attainable density of the bacteria should cause the aggregate spacing to change according to this scaling law. In Ref. [7], a formula for how the maximum density in a collapsed aggregate depends on the initial oxygen concentration C_{Ox} , was derived and shown to be $\rho_m \sim e^{C_{\text{Ox}}}$. This implies that the wavelength of the pattern should decrease exponentially with the oxygen concentration; systematic experiments could test this prediction.

One prediction that can be compared with published experiments is the *lower bound* on the aggregate spacing that follows from the hard-packing density of bacteria. Using the characteristic size $10 \mu\text{m}$ of *E. coli*, the maximum density is approximately $10^9 / \text{cm}^3$. Thus the measured aggregate spacing should always be above the lower bound

$$\lambda_{\min} = 0.1 \text{ mm.} \quad (55)$$

Although admittedly a crude prediction, this lower bound agrees with experiments, where spacings are typically measured in millimeters.

ACKNOWLEDGMENTS

We are grateful to Elena Budrene for teaching us about her experiments that inspired this work and for many useful discussions. We acknowledge discussions with Leonid Levitov, Leo Kadanoff, Shankar Venkataramani, and Martine Benamar, and thank Daniel Fisher for helpful comments. This research was supported by the National Science Foundation Division of Mathematical Sciences and the A. P. Sloan Foundation. M. D. B. acknowledges support from the Program in Mathematics and Molecular Biology at the Florida State University, with funding from the Burroughs Wellcome Fund Interfaces Program.

APPENDIX A: REMARKS ON NUMERICAL METHODS

The partial differential equations described in this paper were solved using second-order in space finite-difference methods, supplemented with adaptive mesh refinement. The time discretization used a θ -weighted Crank-Nicolson-type scheme [i.e., in the equation $\dot{f} = Lf$ the right-hand side is evaluated at time $(n + \theta)\Delta t$, where Δt is the time step]. Typically, in the simulations with one spatial dimension, $\theta = 0.6$. For the simulations in two spatial dimensions, we used an ADI operator splitting method, which requires using $\theta = 1$. Because these methods are implicit, at each time step a matrix inversion was necessary. This is the most expensive part of the numerical method.

The most subtle aspect of the numerical simulations reported in this paper is the mesh refinement. Without good mesh refinement it is impossible to get close enough to the singularity to resolve the collapse; without good mesh refinement in the two-dimensional simulations it would be impossible to acquire enough decades of data to test the phase-equation theory presented in Sec. IV. The philosophy of mesh refinement employed in this paper (first explained to us by Eggers) is to frequently implement gradual changes in the mesh, as opposed to infrequently implementing large changes.

Cylindrical collapse (one spatial dimension). We used a scheme in which mesh refinement is implemented every time the maximum density increases by 1%. During the refinement, the characteristic scale over which the solution varies is determined, and a mesh is constructed to resolve this scale; typically, this involves making sure there are at least 100 mesh points across the region where the solution varies significantly. The solution on the new mesh is constructed by cubic spline interpolation of the old mesh. Because the mesh is refined frequently, the changes to the solution occurring during refinement are small, and there are no convergence difficulties after refinement. The algorithm allows us to find solutions over essentially arbitrary changes in the bacterial density with as few as 200 mesh points.

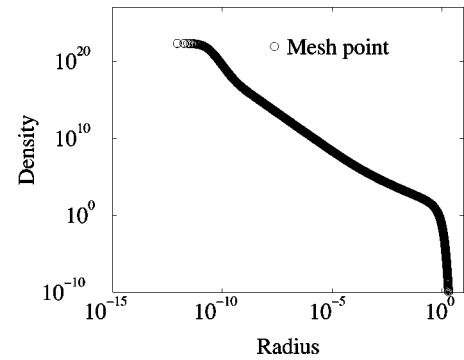


FIG. 10. Plot of one of the density profiles from Fig. 3, showing each mesh point.

We tested the algorithm on the three-dimensional problem (spherical collapse) and confirmed that the results agree with the known analytic solution to extremely good accuracy.

Two spatial dimensions. In two dimensions, the equations were solved with a position grid by using standard operator splitting techniques. The mesh is rectangular, and described by two functions, the x coordinate x_i and the y coordinate y_j . Because the one-dimensional algorithm described above can achieve good resolution with a few hundred mesh points, it is possible to resolve density changes in two spatial directions by using of order 10^4 mesh points. The algorithm for these simulations is analogous to that for the one-dimensional case described above: every 50 time steps, the x grid (or y grid) is remeshed, in accordance with the criteria outlined above. Typically we stagger the remeshing between the two directions by 25 time steps.

Both the one- and two-dimensional codes were tested extensively by checking the solutions against known analytical results. For the one-dimensional code, significant problems were found when simulating cylindrical collapse, as discussed in the next section. All of the results presented in this paper follow the philosophy that numerical results are only believable if they can be replicated by asymptotic solutions of the equations. For the two-dimensional code, one might worry that the operator splitting coupled with the remeshing induces artificial biases in the numerics; we also tested the two-dimensional code by checking that it can reproduce the scalings and the similarity solution for spherically symmetric collapse, where the solution is well known.

APPENDIX B: NUMERICAL DIFFICULTIES FOR CYLINDRICAL COLLAPSE

Our attempts to capture numerically the logarithmic corrections to the cylindrical collapse encountered difficulties. Here we describe our results and pose this problem as an open question. We begin by recalling a theorem concerning the cylindrical collapse of Eqs. (3), (4): self-similar solutions satisfying the boundary conditions (stationarity at infinity) do not exist.

Our numerical calculations identified discrete solutions that violate this theorem even as the mesh spacing tends to zero. Our simulations showed very high resolution of the density and concentration profiles, as shown in Figs. 3 and 4;

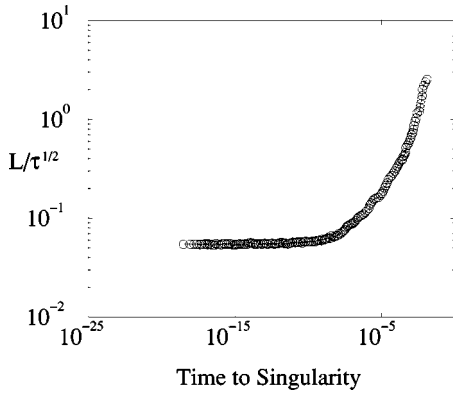


FIG. 11. Spurious logarithmic corrections in the radial grid simulation. Plot of the length scale L divided by $\tau^{1/2}$ for the simulation shown in Figs. 3 and 4. The apparent constant value close to the singularity is a result of the remeshing and interpolation scheme, which does not conserve mass.

we have replotted one density profile from Fig. 3 showing the mesh points used in the simulation (Fig. 10). This high resolution is maintained uniformly throughout the simulations by our remeshing procedure: if we plot the profile at any time in similarity variables, the profile resembles that of Fig. 10. Our numerical method is putatively second-order accurate. Although the remeshing complicates the error prediction, we would naively guess that by maintaining a well-resolved profile in similarity variables, we achieve second-order accuracy in similarity variables.

The apparent logarithmic correction we find is shown in Fig. 11, where we plot $L/\sqrt{\tau}$ vs τ . The simulation, in fact, shows that as $\tau \rightarrow 0$, there is no correction. After an initial transient phase, we find that $L/\sqrt{\tau}$ is constant, as expected in the absence of a logarithmic correction. Initially, we thought that plots like Fig. 11 were evidence for very slow ($\log \log \tau$) corrections, as observed for the nonlinear Schrödinger equation [47]. However, we realized that these results may be biased by our remeshing and interpolation procedures, which are not mass-conserving. As a result, the remeshing reduces the total mass of the system in a roughly self-similar fashion. We therefore wondered if remeshing affects the features of Fig. 11. We found that changing the frequency of remeshing (which changes the rate of “numerical mass loss”) changes Fig. 11, indicating that the result is an artifact.

After discovering this problem, we switched to a numerical scheme based on a mass grid. Here, the initial grid is uniformly spaced in mass increments, and the density and the radius are solved as functions of the mass. We took $\epsilon = 0$ in Eq. (4), so the radius is related to the mass by

$$r \frac{\partial r}{\partial m} = \frac{1}{\rho}. \quad (\text{B1})$$

The boundary conditions used were $r=0$ at the origin, reflection symmetry of the density about $r=0$, and constant density at the outer boundary. The code based on a mass grid does not necessarily require remeshing. The initial grid points between $m=0$ and $m=4$ track the inner collapsing region automatically. Apart from the change of variables, this

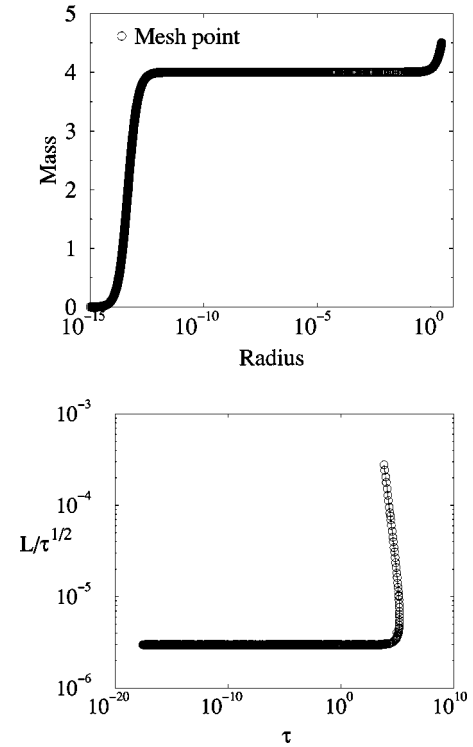


FIG. 12. Cylindrical collapse with a mass grid. Top, mass as a function of radius. Bottom, the length scale L divided by $\tau^{1/2}$. This simulation has a total mass = 4.5 and an 10^5 initial grid points.

code used the same type of integration (discussed in Appendix A) as the radial-grid code.

In addition, we add mesh points to the simulation in regions where the mass changes slowly with the radius. We find this type of behavior just outside the collapsed region, where the mass is nearly equal to 4 over several decades in radius. We add mesh points to avoid numerical errors caused by the loss of resolution when neighboring grid points have very different radii. We used different criteria, for example, we added more points whenever the radial spacing between neighboring mesh points was larger than some threshold, or whenever the fractional density difference between neighboring mesh points was above some threshold.

Our results showed similarly well-resolved profiles as the radial-grid results. In particular, we show in Fig. 12 a profile of the mass vs radius for a time near the singularity. Note that the plotted points are dense over the many decades where the mass changes slowly with radius, confirming the success of the procedure described above.

The scaling of $L/\sqrt{\tau}$ in the mass-grid simulation is also shown in Fig. 12. The plot shows no logarithmic corrections; after an initial transient $L/\sqrt{\tau}$ is constant.

Despite the high resolution shown in our plots, we were suspicious of the results of the mass-grid simulation because the $L/\sqrt{\tau}$ curve is time-independent over 20 decades, suggesting the existence of a similarity solution (in violation of the aforementioned theorem). We looked for numerical artifacts by changing the number of mesh points N , and found changes in our results. For example, the singular time—the time at which the density becomes infinite—varies logarithmically with N .

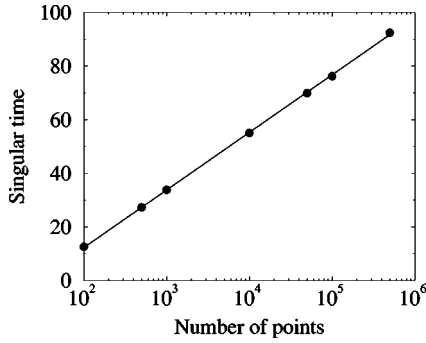


FIG. 13. The singular time in the simulation vs number of grid points. The solid line shows a logarithmic fit to the points. The simulations used a mass grid with total mass $M=4.5$ and boundary conditions as described in the text.

mically with the number of points N (Fig. 13). We do not understand why the singular time found by our supposedly second-order method varies as $\ln N$.

It is noteworthy that these results disagree with the theory of Herrero and Velazquez [26], who predict that the form of the logarithmic correction is

$$\frac{L}{\sqrt{\tau}} \sim \exp(-\sqrt{2}/2\sqrt{|\ln \tau|}). \quad (\text{B2})$$

This form is a strong log correction that we thought would be observable in our simulations. We do not know if the disagreement is because of the inadequacies of our numerics; this is an interesting problem for future research.

APPENDIX C: PHASE EQUATION FOR A BACTERIAL CYLINDER

In this section, we fill in the details of the calculation of the phase equation. Evaluating the coefficients in Eq. (28), we find [48]

$$F(R_0, C_0) = R_0 + \frac{\eta R'_0}{2}, \quad (\text{C1})$$

$$G(R_0, C_0) = R_0 + \frac{\eta R'_0}{2} - \frac{\eta R_0 C'_0}{2}, \quad (\text{C2})$$

$$H(R_0, C_0) = 2R_0 + \frac{1}{4}[7\eta R'_0 + \eta^2 R''_0 - 5\eta R_0 C'_0 - \eta^2 (R_0 C'_0)']. \quad (\text{C3})$$

To evaluate the solvability condition, we need to find the zero mode of the adjoint to the operator Λ found by linearizing the original equations. In this case, Λ is the matrix

$$\begin{pmatrix} \nabla^2 - \nabla \cdot (\nabla C_0 \cdot) & -\nabla \cdot (R_0 \cdot) \\ 1 & \nabla^2 \end{pmatrix}. \quad (\text{C4})$$

All of the terms in Λ are self-adjoint except those of the form $\nabla \cdot (\nabla C_0 \cdot)$. Under the definition (for a cylinder of bacteria) of the inner product $\langle f, g \rangle = \int r dr \int dz f g$, we find the adjoint

$$[\nabla \cdot (\nabla C_0 \cdot)]^\dagger = -\partial_r C_0 \partial_r, \quad (\text{C5})$$

which gives the adjoint linear operator

$$\Lambda^\dagger = \begin{pmatrix} \nabla^2 + \nabla_r C_0 \nabla_r & 1 \\ -\nabla \cdot (R_0 \nabla \cdot) & \nabla^2 \end{pmatrix}. \quad (\text{C6})$$

This linear operator possesses a simple zero mode: $\Lambda^\dagger(1, 0) = 0$. The coefficients of the phase equation thus become

$$c_1 = \langle 1, F(R_0, C_0) \rangle, \quad (\text{C7})$$

$$c_2 = \langle 1, G(R_0, C_0) \rangle, \quad (\text{C8})$$

$$c_3 = \langle 1, H(R_0, C_0) \rangle. \quad (\text{C9})$$

A subtlety comes when we evaluate the inner products: we must integrate (in similarity variables) to the limit of validity of the similarity solution. For a cylinder, this upper limit is η_* , the radius at which the solution matches onto the outer solution. From the asymptotics discussed earlier, we use that $\eta_* \sim A^{-1/2} = f(\tau)$. Evaluating the inner products, and taking the limit $\tau \rightarrow 0$, we arrive at the result

$$c_1 = \frac{-4}{f^2}, \quad (\text{C10})$$

$$c_2 = 4, \quad (\text{C11})$$

$$c_3 = -4. \quad (\text{C12})$$

The resulting phase equation is

$$\frac{\tau_t + 1}{f^2} = \tau_{zz} - \frac{\tau_z^2}{\tau}. \quad (\text{C13})$$

[1] *Singularities in Fluids, Plasmas, and Optics*, Vol. 404 of *NATO Advances Study Institute, Series C: Mathematical and Physical Sciences*, edited by Russel E. Caflisch and George C. Papanicolaou (Kluwer Academic Publishers, Dordrecht, The Netherlands, 1993).

[2] A. Pumir and E.D. Siggia, *Phys. Rev. Lett.* **68**, 1511 (1992).

[3] J. Eggers, *Phys. Rev. Lett.* **71**, 3458 (1993).

[4] R.B. Larson, *Mon. Not. R. Astron. Soc.* **145**, 271 (1969).

[5] E.O. Budrene and H.C. Berg, *Nature (London)* **349**, 630 (1991).

[6] E.O. Budrene and H.C. Berg, *Nature (London)* **376**, 49 (1995).

[7] M.P. Brenner, L. Levitov, and E.O. Budrene, *Biophys. J.* **74**,

- 1677 (1995).
- [8] E. Ben-Jacob, I. Cohen, and H. Levine, *Adv. Phys.* **49**, 395 (2000).
- [9] H.C. Berg and L. Turner, *Biophys. J.* **58**, 919 (1990).
- [10] A.J. Wolfe and H.C. Berg, *Proc. Natl. Acad. Sci. U.S.A.* **86**, 6973 (1989).
- [11] S.M. Block and H.C. Berg, *Nature (London)* **309**, 470 (1984).
- [12] D.F. Blair and H.C. Berg, *Science* **242**, 1678 (1988).
- [13] J.E. Segall, S.M. Block, and H.C. Berg, *Proc. Natl. Acad. Sci. U.S.A.* **83**, 8987 (1986).
- [14] M.J. Schnitzer, S. Block, H.C. Berg, and E. Purcell, *Symp. Soc. Gen. Microbiol.* **46**, 15 (1990).
- [15] Mark J. Schnitzer, *Phys. Rev. E* **48**, 2553 (1993).
- [16] R. Tyson, Ph.D. thesis, University of Washington, 1996.
- [17] R. Tyson, S.R. Lubkin, and J.D. Murray, *Proc. R. Soc. London, Ser. B* **266**, 299 (1998).
- [18] E. Ben-Jacob, Inon Cohen, Ofer Shochet, I. Aranson, H. Levine, and L. Tsimring, *Nature (London)* **373**, 566 (1995).
- [19] L. Tsimring, H. Levine, I. Aranson, E. Ben Jacob, I. Cohen, O. Shochet, and W. Reynolds, *Phys. Rev. Lett.* **75**, 1859 (1995).
- [20] D.E. Woodward, R. Tyson, M.R. Myerscough, J.D. Murray, E.O. Budrene, and H.C. Berg, *Biophys. J.* **68**, 2181 (1995).
- [21] W.J. Bruno, *CNLS Newslett.* **82**, 1 (1992).
- [22] V. Nanudjiah, *J. Theor. Biol.* **42**, 63 (1973).
- [23] S. Childress and J.K. Percus, *Math. Biosci.* **56**, 217 (1981).
- [24] E.O. Budrene (private communication).
- [25] S. Childress, *Lect. Notes Biomath.* **55**, 61 (1984).
- [26] M.A. Herrero and Juan J.L. Velazquez, *Math. Ann.* **308**, 583 (1996).
- [27] P. Manneville, *Dissipative Structures and Weak Turbulence* (Academic Press, New York, 1990).
- [28] T.R. Powers, D. Zhang, R.E. Goldstein, and H.A. Stone, *Phys. Fluids* **10**, 1052 (1998).
- [29] H.C. Berg, *Cold Spring Harbor Symp. Quant. Biol.* **53**, 1 (1988).
- [30] J.B. Stock and M.G. Surette, in *Escherichia coli and Salmonella*, edited by Fredrick C. Neidardt (ASM Press, Washington, D.C., 1996), pp. 1103–1129.
- [31] H.C. Berg and D.A. Brown, *Nature (London)* **239**, 500 (1972).
- [32] E.F. Keller and L.A. Segel, *J. Theor. Biol.* **26**, 399 (1970).
- [33] J. D. Murray, *Mathematical Biology* (Springer Verlag, Berlin, 1989).
- [34] G.F. Oster and J.D. Murray, *J. Exp. Zool.* **251**, 186 (1989).
- [35] J. Spudich and D. Koshland, *Nature (London)* **262**, 467 (1975).
- [36] M.P. Brenner, P. Constantin, L.P. Kadanoff, A. Shenkel, and S.C. Venkataramani, *Nonlinearity* **12**, 1071 (1999).
- [37] R.E. Goldstein, *Phys. Rev. Lett.* **77**, 775 (1996).
- [38] G. B. Whitham, *Linear and Nonlinear Waves* (Wiley, New York, 1974).
- [39] The simulation shown here used a box size $W=15$ with a total mass of $M=12$ and $\epsilon=0$. For boundary conditions, we demanded reflection symmetry at the origin and zero flux at the outer boundary. Different initial conditions give similar final results; here we used a Gaussian profile.
- [40] M.C. Cross and P.C. Hohenberg, *Rev. Mod. Phys.* **65**, 851 (1993).
- [41] Joseph B. Keller and John S. Lowengrub, in *Singularities in Fluids, Plasmas and Optics*, edited by R.E. Caflisch and G.C. Papanicolaou (Kluwer, Dordrecht, The Netherlands, 1993), pp. 111–129.
- [42] A. J. Bernoff (private communication).
- [43] The inner product here is $\langle f, g \rangle = \int r dr \int dz f g$. The functions are all real.
- [44] For the simulations presented in this section, the cylinder was represented on a mesh in (r, z) , with boundary conditions that $\rho(W)=0$ and $c(W)=0$, with W a fixed constant ($W=5$ in the simulations below). Reflection symmetry was enforced at both $z=0$ and $z=L=20$, so that the solution is periodic in z .
- [45] E.M. Lifshitz and L.P. Pitaevskii, *Physical Kinetics*, Vol. 10 of *Course in Theoretical Physics* (Pergamon Press, New York, 1981).
- [46] Note that the estimate for the chemotactic coefficient given in Ref. [7] has an algebraic error.
- [47] G. Fibich and G. Papanicolaou, *SIAM (Soc. Ind. Appl. Math.) J. Appl. Math.* **60**, 183 (1999).
- [48] The values of coefficients here were computed with $f(\tau)=1$ for simplicity. When f varies in time, there will be slight differences in the numerical values of the coefficients; however, these coefficients remain constant in time and the qualitative behavior of the phase equation is unchanged.